



## The $k$ - $\epsilon$ - $f_p$ model applied to double wind turbine wakes using different actuator disk force methods

Laan, van der, Paul Maarten; Sørensen, Niels N.; Réthoré, Pierre-Elouan; Mann, Jakob; Kelly, Mark C.; Troldborg, Niels

*Published in:*  
Wind Energy

*Link to article, DOI:*  
[10.1002/we.1816](https://doi.org/10.1002/we.1816)

*Publication date:*  
2015

*Document Version*  
Peer reviewed version

[Link back to DTU Orbit](#)

### *Citation (APA):*

Laan, van der, P. M., Sørensen, N. N., Réthoré, P-E., Mann, J., Kelly, M. C., & Troldborg, N. (2015). The  $k$ - $\epsilon$ - $f_p$  model applied to double wind turbine wakes using different actuator disk force methods. *Wind Energy*, 18(12), 2223–2240. <https://doi.org/10.1002/we.1816>

---

### General rights

Copyright and moral rights for the publications made accessible in the public portal are retained by the authors and/or other copyright owners and it is a condition of accessing publications that users recognise and abide by the legal requirements associated with these rights.

- Users may download and print one copy of any publication from the public portal for the purpose of private study or research.
- You may not further distribute the material or use it for any profit-making activity or commercial gain
- You may freely distribute the URL identifying the publication in the public portal

If you believe that this document breaches copyright please contact us providing details, and we will remove access to the work immediately and investigate your claim.

RESEARCH ARTICLE

# The $k$ - $\varepsilon$ - $f_P$ model applied to double wind turbine wakes using different actuator disk force methods

M. Paul van der Laan<sup>1</sup>, Niels N. Sørensen<sup>1</sup>, Pierre-Elouan Réthoré<sup>1</sup>, Jakob Mann<sup>1</sup>, Mark C. Kelly<sup>1</sup>, Niels Troldborg<sup>1</sup>

<sup>1</sup>Department of Wind Energy, Technical University of Denmark, Risø campus, DK-4000 Roskilde, Denmark.

## ABSTRACT

The newly developed  $k$ - $\varepsilon$ - $f_P$  eddy viscosity model is applied to double wind turbine wake configurations in a neutral atmospheric boundary layer, using a Reynolds averaged Navier-Stokes solver. The wind turbines are represented by actuator disks. A proposed variable actuator disk force method is employed to estimate the power production of the interacting wind turbines and the results are compared with two existing methods; a method based on tabulated airfoil data and a method based on the axial induction from 1D momentum theory. The proposed method calculates the correct power, while the other two methods overpredict it. The results of the  $k$ - $\varepsilon$ - $f_P$  eddy viscosity model are also compared with the original  $k$ - $\varepsilon$  eddy viscosity model and Large-Eddy Simulations. Compared to the LES-predicted velocity and power deficits, the  $k$ - $\varepsilon$ - $f_P$  is superior to the original  $k$ - $\varepsilon$  model. Copyright © 2014 John Wiley & Sons, Ltd.

## KEYWORDS

$k$ - $\varepsilon$  eddy viscosity model; wind turbine wake interaction; actuator disk; CFD; RANS; LES.

## Correspondence

M. Paul van der Laan, Department of Wind Energy, Technical University of Denmark, Risø campus, DK-4000 Roskilde, Denmark.

Email: plaa@dtu.dk

Received . . .

## 1. INTRODUCTION

In modern wind farms, the interaction of wind turbine wakes can cause annual energy losses of 10 to 20% [1, 2]. In addition, the wake turbulence increases the loading on the wind turbine blades, which may lead to premature failure. Wind turbine wake interaction has been studied numerically by many authors, using models that range from simple engineering wake models such as the N.O. Jensen model [3], to high fidelity Computational Fluid Dynamics (CFD) methods, including Large-Eddy Simulations (LES) [4, 5]. Reynolds-Averaged Navier Stokes (RANS) solvers use a CFD method that is roughly three orders cheaper than the LES [6]. In contradiction to LES, in which the large scale turbulence is resolved in time and only the small turbulent scales are modeled, a RANS method models the averaged turbulent quantities completely, in a steady-state simulation. Many authors [6, 7, 8, 9, 10] have employed the widely used  $k$ - $\varepsilon$  Eddy Viscosity Model (EVM) to model the turbulence in RANS. Their work shows that  $k$ - $\varepsilon$  EVM underpredicts the velocity deficit of a single wind turbine. To overcome this problem, an extended  $k$ - $\varepsilon$  EVM, called the  $k$ - $\varepsilon$ - $f_P$  EVM was developed [6] based on the work of Apsley and Leschziner [11]. The  $k$ - $\varepsilon$ - $f_P$  EVM has a variable  $C_\mu$ , instead of the constant  $C_\mu$ , used in the original  $k$ - $\varepsilon$  EVM. The varying part of  $C_\mu$  is defined by the scalar function  $f_P$ , which is only dependent on local velocity gradients. The variable  $C_\mu$  has lower values compared to the constant  $C_\mu$  in regions where the velocity gradients are high, e.g. the edge of a wind turbine wake. As a result, the turbulent eddy viscosity in the wake is much lower in  $k$ - $\varepsilon$ - $f_P$  EVM compared to the original  $k$ - $\varepsilon$  EVM. Therefore, the  $k$ - $\varepsilon$ - $f_P$  EVM predicts a larger velocity deficit than the  $k$ - $\varepsilon$  EVM. The  $k$ - $\varepsilon$ - $f_P$  EVM includes a parameter  $C_R$  that controls the velocity deficit completely, so  $C_R$  should be chosen with care. In previous work [6],  $C_R$  is calibrated with the velocity deficit predicted by LES, for eight different single wind turbine wake cases. It should be noted that the  $k$ - $\varepsilon$ - $f_P$  EVM can only model isotropic turbulence, and thus cannot predict the anisotropic Reynolds-stresses present in LES and field measurements.

In the present paper, the  $k\text{-}\varepsilon\text{-}f_P$  EVM is applied to two closely spaced wind turbines for different orientations. The wind turbine geometry is not physically modeled, instead the rotor forces are represented by an Actuator Disk (AD) [7, 12, 13]. The AD acts as a momentum source term in the Navier-Stokes equations. Troldborg et al. [14, 15] showed that, as long as the AD is subjected to ambient atmospheric turbulence, the averaged velocity deficit calculated by the AD is similar to that from a CFD simulation in which the full rotor geometry is represented. When multiple ADs are used to simulate wake interaction in wind farms, the force on each AD is not known prior to the simulation. Therefore, it is necessary to have a method for prescribing AD forces that vary during the simulation. In the literature, several variable AD force methods are used [8, 9, 13, 16, 17]; however, it is not clear how these methods compare with each other. The AD forces strongly influence the flow solution, hence it is important to correctly model them. The main aim of the present paper is to find the best setup for simulations of interacting ADs in RANS, which can be used for wind farm simulations in future work. To reach this goal, one new variable AD force method is proposed in Section 2.2 and it is compared with two existing variable AD force methods, for a single and a double wind turbine setup, in Section 4.2.1 and Section 4.2.2, respectively. The velocity deficit calculated by the  $k\text{-}\varepsilon\text{-}f_P$  EVM applied to two wind turbines, is compared with results of the standard  $k\text{-}\varepsilon$  EVM and LES, in Section 4.2.3. In this exercise, the AD forces are kept constant, such that only the turbulence models are compared. In Section 4.2.4, one variable AD force method is used to compare the  $k\text{-}\varepsilon\text{-}f_P$  EVM with the standard  $k\text{-}\varepsilon$  EVM and LES, in terms of the power deficit. An overview of the comparisons is given in Table I. The three variable AD force methods (Methods I-III) are discussed in Section 2 and the individual test cases (cases 1-7) are described in Section 3.

**Table I.** Overview of comparisons.

Section	Single/double wakes	Test case(s)	Variable AD force method(s)	Turbulence model(s)
4.2.1	single	1	Methods I-III	$k\text{-}\varepsilon\text{-}f_P$ EVM
4.2.2	double	6-7	Methods I-III	$k\text{-}\varepsilon\text{-}f_P$ EVM
4.2.3	double	2-5	none	$k\text{-}\varepsilon$ EVM, $k\text{-}\varepsilon\text{-}f_P$ EVM and LES
4.2.4	double	6-7	Method I	$k\text{-}\varepsilon$ EVM, $k\text{-}\varepsilon\text{-}f_P$ EVM and LES

## 2. FORCE TREATMENT FOR MULTIPLE ACTUATOR DISKS

The wind turbine geometry is not present in the flow simulations. Instead, the rotor forces are modeled with an actuator disk (AD) [7, 12, 13]. The AD acts as a momentum sink in the Navier-Stokes equations. The force loading of AD determines the amount of momentum that is extracted from the flow and is therefore very important in wind turbine wake simulations, that are modeled with ADs. Different types of AD loading are proposed in the literature. The most simple approach is a uniformly distributed loading, in which only the total amount of the normal force  $F_N$  is modeled and it is kept constant during the simulations [7, 10]:

$$F_N = \frac{1}{2}\rho C_T A U_{H,\infty}^2, \quad (1)$$

with  $\rho$  as the air density,  $C_T$  as the thrust coefficient,  $A = \pi R^2$  as the rotor area with  $R$  as the blade radius and  $U_{H,\infty}$  as the free-stream velocity at hub height. In addition, one could add a uniformly distributed tangential force component, in which the total magnitude is determined by the torque  $\tau$ :

$$\tau = \frac{P}{\Omega} = \frac{\frac{1}{2}\rho C_P A U_{H,\infty}^3}{\Omega}, \quad (2)$$

where  $P$  is the wind turbine power,  $\Omega$  is the rotational speed in radians per second and  $C_P$  is the power coefficient. Instead of using a uniformly distributed normal and tangential force distribution, it is also possible to scale a reference blade force distribution with the parameters defined in equations (1,2). In previous work [6], this method is used to scale the normal blade force distribution  $q_N(r)$  and the tangential blade force distribution  $q_T(r)$  of the NREL 5-MW reference wind turbine [18], to represent rotor forces of different wind turbines. Note that  $r$  is the radial coordinate of the blade. The normalized  $q_N(r)$  and  $q_T(r)$  of the NREL 5-MW reference wind turbine are plotted in Figure 1. The scaling of the reference distribution is as defined in van der Laan et al. [6]:

$$\begin{aligned} q_N^{AD}(r) &= \hat{q}_N(r) \frac{1}{n} \frac{1}{2} \rho U_{H,\infty}^2 \pi R^2 C_T, & \hat{q}_N(r) &= \frac{q_N(r)}{\int_0^R q_N(r) dr}, \\ q_T^{AD}(r) &= \hat{q}_T(r) \frac{1}{n} \frac{1}{2} \rho U_{H,\infty}^3 \frac{\pi R^2 C_P}{\Omega}, & \hat{q}_T(r) &= \frac{q_T(r)}{\int_0^R q_T(r) r dr}, \end{aligned} \quad (3)$$

where the superscript AD denotes the scaled AD blade force distribution,  $\hat{q}$  is a normalized blade force distribution and  $n$  is the number of blades. The use of a reference blade force distribution implies that the shape of the blade force distribution (normalized by  $0.5\rho R U_{H,\infty}^2$ ) should not change much with different free-stream velocities and different blades. The assumption might be violated for a wind turbine blade that is very different in geometry compared to the reference blade or if the simulated turbine operates at conditions far from those in which the reference loading was obtained. However, a similar assumption is made when tabulated airfoil data is used for the AD forces, to represent a wind turbine rotor from which the actual blade geometry and corresponding aerodynamics are unknown. This assumption is used by Porté-Agel et al. [19] and Churchfield et al. [4]. In their work the AD forces of the Siemens SWT-2.3-93 wind turbine are modeled by using a newly designed wind turbine, that mimics the known power production.

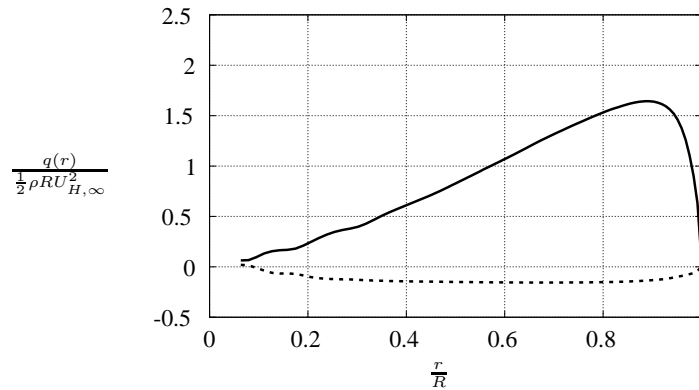


**Figure 1.** Calculated tangential  $q_T(r)$  (dashed line) and normal force  $q_N(r)$  (solid line) distributions.

The determination of the actuator disk forces in multiple wake configurations is not trivial. In the cases where downstream ADs feel the velocity deficit of upstream ADs, the total force cannot be constant for all ADs. Instead, the downstream ADs that are positioned in the full wake of others, should experience lower normal and tangential forces compared to those that are subject to the undisturbed flow.

When the AD loading is based on uniformly distributed forces equations (1,2) or a scaled reference distribution equation (3), information of the force scaling coefficients  $C_T$ ,  $C_P$ ,  $\Omega$  and the free-stream velocity  $U_{H,\infty}$  is necessary to obtain the correct total forces.  $C_T$ ,  $C_P$ ,  $\Omega$  are often defined as function of  $U_{H,\infty}$ , hence, when  $U_{H,\infty}$  is known for a particular AD, the corresponding AD forces can be determined. However,  $U_{H,\infty}$  is not known for an AD that is in the lee of another. This problem is approached by a simple existing method and an alternative proposed method in Section 2.1 and Section 2.2, respectively. In addition, another existing variable force method, in which tabulated airfoil data is used instead of a reference force distribution of Figure 1, is described in Section 2.3.

## 2.1. Method I: AD Induction Method

One could consider to estimate the free-stream velocity  $U_{H,\infty}$  by the axial induction factor  $a_x$  from 1D momentum theory, as performed in the work of Prospathopoulos [9] et al., Calaf et al. [16] and used by Wu and Porté-Agel [17] for an actuator disk model that does not include rotation (ADM-NR):

$$a_x = 0.5 \left( 1 - \sqrt{1 - C_T} \right), \quad (4)$$

$$U_{H,\infty} = \frac{\langle U_{AD} \rangle}{1 - a_x},$$

with  $\langle U_{AD} \rangle$  as the local velocity at the AD, averaged over the whole AD area  $A$ , which can be extracted from the flow field. Prior to the first iteration in CFD,  $U_{H,\infty}$  is guessed based on the free-stream wind speed, which provides the scaling coefficients  $C_T$ ,  $C_P$  and  $\Omega$ , that determine the AD forces. After the first iteration,  $\langle U_{AD} \rangle$  is probed at the AD and a new  $U_{H,\infty}$  is calculated with equation (4). Subsequently, the scaling coefficients and AD forces are updated. The iteration process is repeated until the forces are converged to a satisfactory level. Prospathopoulos et al. [9] proposed an extra empirical relation for  $C_T(a_x)$  for large induction factors,  $a_x > 0.4$  but in the current work it is observed that the converged induction factor is never larger than 0.4. Note that Prospathopoulos et al. only used a uniformly distributed normal force, as defined by equation (1).

## 2.2. Method II: AD Variable Scaling Method

In the present research, an alternative variable force method is proposed. Using a calibration procedure of single wind turbine wake simulations, it is possible to calculate alternative scaling coefficients  $C_T^*$ ,  $C_P^*$  and  $\Omega^*$ , that represent  $C_T$ ,  $C_P$  and  $\Omega$  as function of a local velocity average around the AD:  $\langle U_{AD} \rangle$ . The alternative scaling coefficients can be used to scale the AD forces dynamically during the simulation by probing  $\langle U_{AD} \rangle$  at the AD. In Method II the scaled AD forces of equation (3) are defined as:

$$\begin{aligned} q_N^{AD}(r) &= \hat{q}_N(r) \frac{1}{n} \frac{1}{2} \rho \langle U_{AD} \rangle^2 AC_T^*, \\ q_T^{AD}(r) &= \hat{q}_T(r) \frac{1}{n} \frac{1}{2} \rho \langle U_{AD} \rangle^3 \frac{AC_P^*}{\Omega^*}, \end{aligned} \quad (5)$$

Hence:

$$C_T^* = C_T \left( \frac{U_{H,\infty}}{\langle U_{AD} \rangle} \right)^2, \quad C_P^* = C_P \left( \frac{U_{H,\infty}}{\langle U_{AD} \rangle} \right)^3 \quad (6)$$

In the calibration procedure, twenty-two single wind turbine simulations for  $4 \leq U_{H,\infty} \leq 25$  with equidistant intervals of 1 m/s are performed to determine  $C_T^*$ ,  $C_P^*$  and  $\Omega^*$  as function of  $\langle U_{AD} \rangle$ . The numerical setup for the single wind turbine simulations is described in detail in the work of van der Laan et al. [6] and a summary is given in Section 4.1.1. In addition, a new calibration is carried out whenever the turbulence model or the ambient turbulence intensity is changed. The calibration of the NREL 5-MW wind turbine from Sec.3 is shown in Figure 2. The calibrated scaling coefficients  $C_T^*$ ,  $C_P^*$  and  $\Omega^*$  are plotted as a function of the averaged AD velocity  $\langle U_{AD} \rangle$ . Four different calibrations are given that differ in turbulence model and ambient turbulence intensity. The dependency of turbulence intensity on the calibration is very small, whereas the calibration is sensitive to the turbulence model. This sensitivity is caused by the difference in the predicted  $\langle U_{AD} \rangle$ , which is most visible in  $C_T^*$  and  $C_P^*$  in the low wind speed range. The effect is small for  $\Omega^*$ .

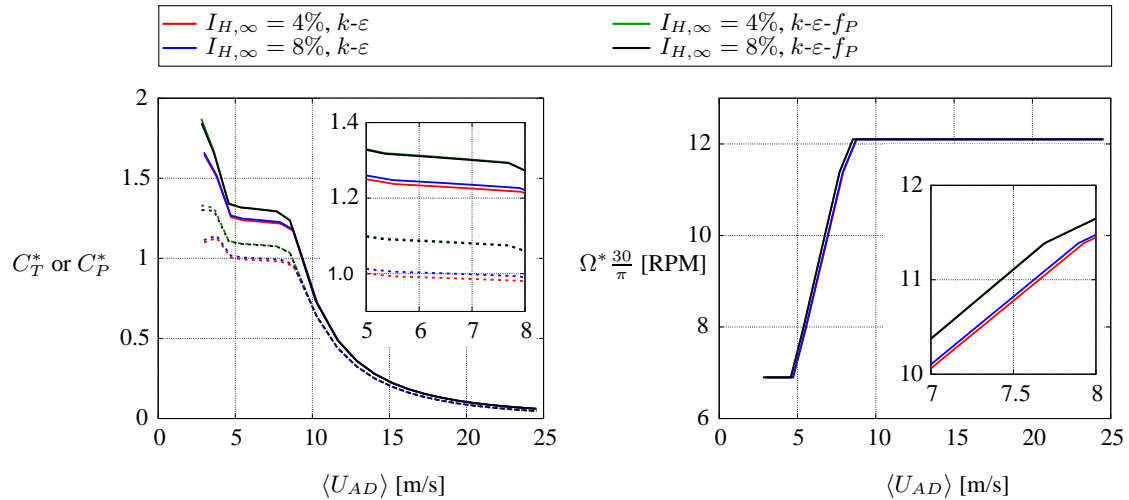


**Figure 2.** Calibration of NREL 5-MW wind turbine. Left:  $C_T^*$  (solid line) and  $C_P^*$  (dashed line). Right: rotational speed  $\Omega^*$  in RPM.

The variable force method has been checked to assure that the correct power, thrust force and rotational speed are obtained, when the calibrated  $C_T^*$ ,  $C_P^*$  and  $\Omega^*$  are used. The error in the power, thrust force and rotational speed are negligible, if the grid of the calibration procedure is the same as the one that is used to verification simulation. If the AD is moved in the grid of the verification simulation, with respect to the AD that was used for the calibration, the error in power is larger but still below 1%. These good results are achieved when the AD is placed in the cell centers.

## 2.3. Method III: AD Airfoil Method (with torque calibration)

A common method to represent the rotor forces on an AD is the use of tabulated airfoil data. This method is based on blade element momentum theory and it is introduced by Sørensen and Shen [20] for the actuator line technique. In later work, the method is used for AD simulations by El Kasmi and Masson [8], Réthoré et al. [13], Wu and Porté-Agel [17]

and others. In the present work, the implementation of Réthoré et al. [13] is used, which can be summarized as:

Force vector:	$\mathbf{f} = \mathbf{L} + \mathbf{D} = \frac{1}{2} \rho U_{rel}^2 \frac{nc}{2\pi r} F (c_l \mathbf{e}_l + c_d \mathbf{e}_d),$
Relative velocity:	$U_{rel} = \sqrt{U_x^2 + (\Omega r - U_\theta)^2},$
Angle between $U_{rel}$ and rotor plane:	$\varphi = \tan^{-1} \left( \frac{U_x}{\Omega r - U_\theta} \right),$
Angle of attack:	$\alpha = \varphi - \gamma,$
Tip correction factor of Shen et al. with modified $c_2$ :	$F = \frac{2}{\pi} \arccos(\exp[-gf]),$
	$g = \exp(-c_1(n\lambda - c_2)) + c_3,$
	$f = \frac{n}{2} \frac{R-r}{r \sin \varphi},$
	$c_1 = 0.125, c_2 = 27, c_3 = 0.1.$

The variables are defined on a cross sectional element at a radial blade coordinate  $r$  in the  $\theta$ - $x$  plane, as shown in Figure 3. Note that  $\theta$  is the azimuthal coordinate and  $x$  is the axial coordinate. In equation (7), the force vector per unit area  $\mathbf{f}$  is the sum of the lift force  $\mathbf{L}$  and the drag force  $\mathbf{D}$ . The orientation of the lift and drag force is defined by the corresponding unit vectors  $\mathbf{e}_l$  and  $\mathbf{e}_d$ , respectively. The force vector  $\mathbf{f}$  depends on the density  $\rho$ , the relative velocity  $U_{rel}$ , the number of blades  $n$ , the chord length  $c$ , the radial location on the blade  $r$  and the sectional lift and drag coefficients  $c_l$  and  $c_d$ , respectively, taken from the tabulated airfoil data. The relative velocity  $U_{rel}$  is defined from the velocity triangle, as sketched in Figure 3, that is a function of the axial velocity  $U_x$ , the rotational velocity  $U_\theta$ , the angular rotational speed  $\Omega$  in radians per second and the radial coordinate  $r$ .  $\varphi$  is the angle between  $U_{rel}$  and the rotor plane that, together with the local pitch angle  $\gamma$  (sum of the blade pitch angle and local twist), defines the local angle of attack  $\alpha$ . To account for a finite number of the blades, the tip correction of Shen et al. [21, 22] used, in which  $\lambda$  is the tip speed ratio,  $R$  is the blade radius and  $c_i$  are empirical constants. Shen et al. determined the constants  $c_i$  from a calibration with two small experimental wind turbine rotors that have a relatively blunt tip, leading to  $c_2 = 21$ . Trolldborg [23] found that for modern large wind turbines with a sharp tip,  $c_2$  should be set to 27, which will be adopted in the present research.

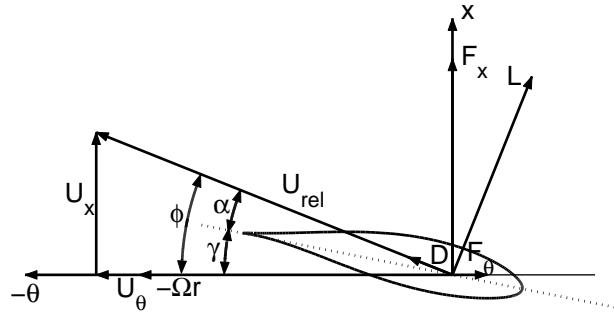


Figure 3. Sectional airfoil element with velocity and force vectors. Source: Réthoré et al. [13].

Réthoré et al. [13] validated the AD with tabulated airfoil data with full rotor computations of a single NREL 5-MW reference wind turbine. Reasonable agreement was found, however, the AD with tabulated airfoil data overpredicted the tangential forces, which resulted into an overpredicted power. In the present work, the AD with tabulated airfoil data is applied to wind turbines in wake conditions. Since the free-stream velocity is not known for wind turbine that is the lee of another, the rotational speed and the pitch are not known prior to the simulation, unless they are constant with wind speed. Unfortunately, any form of wind turbine control, e.g. a torque-controller or pitch controller, is not available for the present research. Instead, a relationship of the torque  $\tau$  and the rotational speed  $\Omega$  is derived, through a calibration of a number of single wind turbine simulations with different free-stream velocities, as performed in the work of Wu and Porté-Agel [24]. The calibration setup is similar to the one that used for Method II from Section 2.2. The  $\tau$ - $\Omega$  relationship can be used to calculate  $\Omega$  during the simulation, in an iterative manner. At the first time step  $\Omega$  is guessed, which gives a value for  $\tau$ . Subsequently, a new  $\Omega$  is obtained from the  $\tau$ - $\Omega$  relationship and it is used for the second time step. The process is repeated until a satisfactory level of convergence is reached. Although, not mentioned by Wu and Porté-Agel, the use of a  $\tau$ - $\Omega$  relationship without a pitch controller only makes sense for the wind speed region in which the blade pitch  $\theta_p$  is zero. If the blade pitch is not zero, one still needs to know the free-stream velocity in order to get the pitch from the pitch curve, such that the correct forces are obtained. Alternatively, if one could define two separate regions, in which either rotational speed control or pitch control is applied, it is possible to derive a corresponding  $\tau$ - $\Omega$  and a  $\tau$ - $\theta_p$  relation, through

calibration. During the simulation, the wind turbine determines which relation it should use by a switch that is based on the torque. In the present work, only a  $\tau\text{-}\Omega$  relationship is used for simplicity, by setting the zero pitch, which is true for the NREL 5-MW wind turbine operating at free-stream wind speeds between 5-11 m/s.

Four results of the  $\tau\text{-}\Omega$  relationship are plotted in Figure 4, representing ambient turbulence intensities of 4% and 8% using two RANS turbulence models: the  $k\text{-}\varepsilon$  EVM and  $k\text{-}\varepsilon\text{-}f_P$  EVM. Figure 4 shows that the calibration is only sensitive to the turbulence model, as found for Method II from Section 2.2. The use of a  $\tau\text{-}\Omega$  relationship has the advantage that the power is no longer overpredicted, since it is calibrated with the desired power curve.

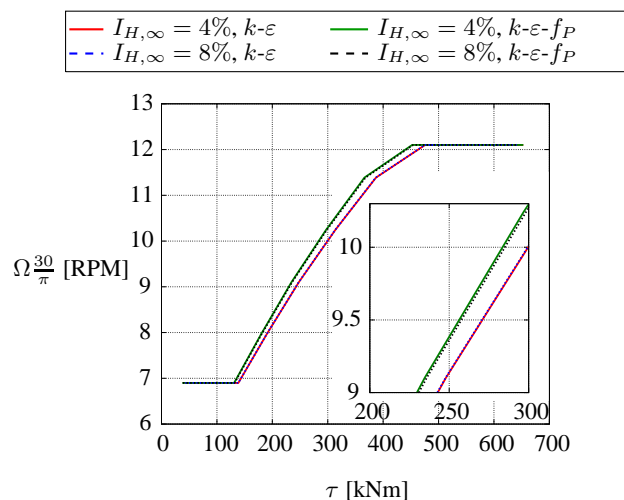


Figure 4.  $\tau - \Omega$  relationship for the NREL 5-MW wind turbine.

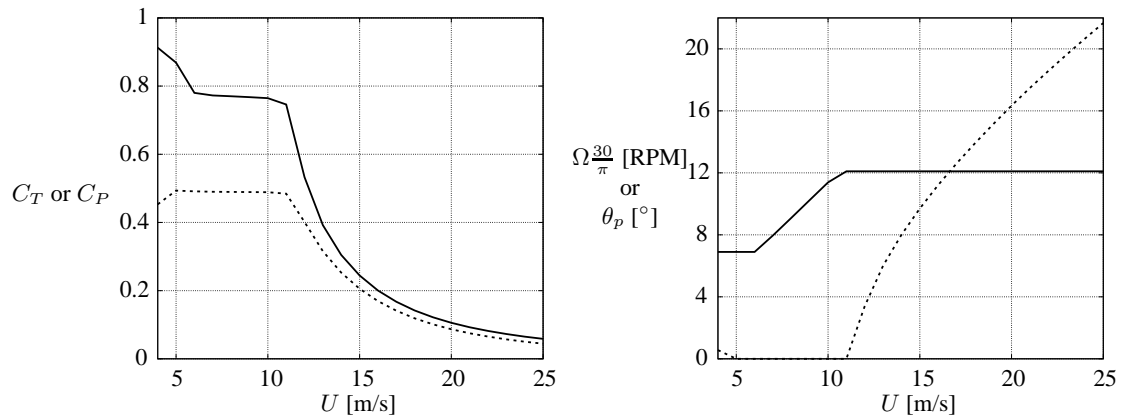
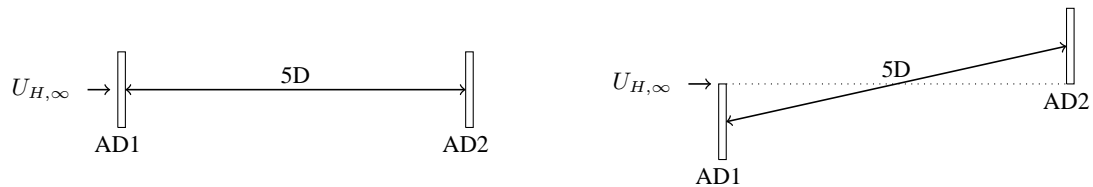
### 3. TEST CASES

The variable AD force methods of Section 2 and three different turbulence models presented in Section 4.1, are tested with seven test cases, as shown in Table II. All test cases are based on the NREL 5-MW reference wind turbine [18], which has a rotor diameter  $D$  of 126 m and a hub height  $z_H$  of 90 m. The thrust coefficient  $C_T$ , the power coefficient  $C_P$ , the rotational speed  $\Omega$  and the blade pitch angle  $\theta_p$  are calculated with the aeroelastic code HAWCStab2 [25], and the results are plotted in Figure 5. HAWCStab2 couples the blade element momentum method with finite beam elements. The first test case is a single wind turbine and it is used to compare the variable AD force methods in terms of power production and thrust force, for a range of free-stream velocities at hub height  $U_{H,\infty}$ . The first four double wake cases are meant to compare the velocity deficit predicted by the  $k\text{-}\varepsilon\text{-}f_P$  EVM and  $k\text{-}\varepsilon$  EVM, with the one calculated by LES for double wake configurations, using constant AD forces. It is chosen to use constant forces, such that only the turbulence models are compared with respect to the flow around the same obstacles. Since everything is known about the LES, e.g. ambient turbulence levels, forces of the wind turbine, etc., these four test cases are ideal to investigate the performance of the  $k\text{-}\varepsilon$  EVM and the  $k\text{-}\varepsilon\text{-}f_P$  EVM for double wake configurations. The last double wake cases are used to compare the three turbulence models in terms of power deficit. In these cases, one variable AD force method is used.

All double wake cases are simulated with  $U_{H,\infty} = 8$  m/s and have a spacing of five rotor diameters. The wind turbine spacing could represent the first two wind turbine in the Lillgrund off-shore wind farm, located in Sweden, for northern wind directions [26]. The influence of the ambient turbulence intensity  $I_{H,\infty}$  is investigated by using 8% for the odd cases and 4% for the even cases. Note that  $I_{H,\infty} \equiv \sqrt{2/3k}/U_{H,\infty}$  represents the total turbulence intensity, with  $k$  as the turbulent kinetic energy. In addition, the position of the wind turbines in the double wake cases is investigated. In the double wake cases with constant AD forces, two orientations are chosen with a spacing of 5D: an aligned and a staggered layout, as sketched in Figure 6. The position in the last two double wake cases is changed for a number of simulations, representing relative wind directions between  $0^\circ$  and  $24^\circ$ .

**Table II.** Summary of cases and corresponding input parameters for numerical computations.

Case	Description	$I_{H,\infty}$ [-]	$U_{H,\infty}$ [m/s]	spacing [m/D]
Single wake, variable forces				
1	NREL 5-MW	8%	4-25	-
Double wake, constant forces, one wind direction				
2	NREL 5-MW aligned, low $I_{H,\infty}$	4%	8	5
3	NREL 5-MW aligned, high $I_{H,\infty}$	8%	8	5
4	NREL 5-MW staggered, low $I_{H,\infty}$	4%	8	5
5	NREL 5-MW staggered, high $I_{H,\infty}$	8%	8	5
Double wake, variable forces, relative wind direction range: $-24^\circ, 24^\circ$				
6	NREL 5-MW low $I_{H,\infty}$	4%	8	5
7	NREL 5-MW high $I_{H,\infty}$	8%	8	5

**Figure 5.** NREL 5-MW wind turbine. Left:  $C_T$  (solid line) and  $C_P$  (dashed line). Right: rotational speed  $\Omega \frac{30}{\pi}$  in RPM (solid line) and blade pitch angle  $\theta_p$  (dotted line).**Figure 6.** Sketch of double wake cases 2-5. Left: aligned and right: staggered.

## 4. SIMULATIONS

The test cases from Table II are simulated in the present section. The simulation methods and results are discussed in Section 4.1 and Section 4.2, respectively.

### 4.1. Method

The RANS and LES are computed with EllipSys3D [27, 28], the in-house incompressible finite volume code of DTU Wind Energy. EllipSys3D solves the Navier-Stokes equations with the SIMPLE algorithm [29] and the convective terms are treated by the QUICK scheme [30]. The flow variables are stored in the cell centers, which can cause decoupling of the pressure with body forces. A modified Rhie-Chow algorithm [31, 32] is used to avoid this decoupling. The setup for the RANS and LES are discussed separately in Section 4.1.1 and Section 4.1.2, respectively.

#### 4.1.1. RANS

The flow domain definition of all seven test cases, as defined in Table II, is the same for all RANS simulations, although the sizes are different. In Figure 7, the grid of test cases 6 and 7 is shown, including the general flow domain definitions that apply for all test cases. In these test cases, the position of the upstream AD is kept constant, while the downstream AD is moved on an arc to model the relative wind directions. To illustrate this, three positions of the downstream AD are sketched in Figure 7, namely at  $0^\circ$ ,  $12^\circ$  and  $24^\circ$ . Around the two ADs, a wake domain is specified in which the cells are uniformly distributed in all directions with a spacing of  $D/10$ . The cell size of  $D/10$  is based on a detailed grid refinement study, performed in previous work [6]. In the  $y$  direction, the wake domain is positioned in the middle of the flow domain. Outside the wake domain, stretching is performed with a maximum cell-edge growth factor of 1.2. The size of the flow domain, the wake domain and the grid sizes are listed in Table III, for all seven test cases. The boundaries at  $x = 0$  and  $z = L_z$  are inlets at which the log law solution is specified:

$$U(z) = \frac{u_*}{\kappa} \ln\left(\frac{z}{z_0}\right), \quad k = \frac{u_*^2}{\sqrt{C_\mu}}, \quad \varepsilon = \frac{u_*^3}{\kappa z}, \quad (8)$$

with  $u_*$  as the friction velocity,  $z_0$  as the wall roughness,  $k$  as the turbulent kinetic energy and  $\kappa = 0.4$  as the Von Karman constant. The ambient turbulence intensity  $I_{H,\infty}$  is set by  $z_0$  while keeping  $C_\mu = 0.03$  constant:

$$I_{H,\infty} \equiv \frac{\sqrt{\frac{2}{3}k}}{U_{H,\infty}} = \frac{\kappa\sqrt{\frac{2}{3}}}{\ln\left(\frac{z_H}{z_0}\right)\sqrt[4]{C_\mu}}, \quad (9)$$

and  $u_*$  is set such that the desired free-stream velocity  $U_{H,\infty}$  at hub height  $z_H$  is obtained. The side boundaries at  $y = 0$  and  $y = L_y$  are slip walls at which a Neumann condition is applied. Note that one could also use periodic boundary conditions, although the difference between the use of periodic or slip boundaries is not significantly noticeable in the wake solution because the boundaries are sufficiently far away. The bottom wall at  $z = 0$  is a rough wall at which the turbulent dissipation and the wall stress are specified at the first cell and a Neumann boundary condition is used for the turbulent kinetic energy. To keep the total number of cells low (1.2 million for test cases 6 and 7), the height of the first cell is set to 0.5 m. An outlet is used at the end of the domain, at  $x = L_x$ , assuming fully developed flow.

**Table III.** RANS flow domain definition of all test cases. Domain sizes and AD coordinates are normalized by the rotor diameter  $D$ .

Case	Description	Flow domain			Wake domain				Upstream AD		Downstream AD	
		$L_x$	$L_y$	$L_z$	$l_x$	$l_y$	$l_z$	$l_{x,up}$	$AD_x$	$AD_y$	$AD_x$	$AD_y$
Single wake, variable forces												
1	NREL 5-MW	25	16	16	12	3	3	2	5	8	-	-
Double wake, constant forces, one wind direction												
2-3	NREL 5-MW aligned	25	20	16	16	6	3	2	5	8	10	8
4-5	NREL 5-MW staggered	25	20	16	16	6	3	2	5	7.5	10	8.5
Double wake, variable forces, relative wind direction range: $-24^\circ, 24^\circ$												
6-7	NREL 5-MW	25	20	16	14	6	3	2	5	8.5	variable	variable

Two RANS turbulence models are investigated; the standard  $k\text{-}\varepsilon$  EVM, first introduced by Launder and Spalding [33], and the  $k\text{-}\varepsilon\text{-}f_P$  EVM that is developed in previous work [6]. Both turbulence models use the Boussinesq approximation [34] for the Reynolds-stresses  $\overline{u'_i u'_j}$ :

$$\overline{u'_i u'_j} = \frac{2}{3}k\delta_{ij} - \nu_T (U_{i,j} + U_{j,i}), \quad (10)$$

where  $\delta_{ij}$  is the Kronecker delta,  $U_{i,j}$  are the mean velocity gradients and  $\nu_T$  is the turbulent eddy viscosity:

$$\nu_T = C_\mu f_P \frac{k^2}{\varepsilon}, \quad (11)$$

with  $C_\mu$  as a constant and  $\varepsilon$  as the turbulent dissipation. In the standard  $k\text{-}\varepsilon$  EVM  $f_P = 1$  and in  $k\text{-}\varepsilon\text{-}f_P$  EVM  $f_P$  is a scalar function that is dependent on the local shear parameter:  $\sigma \equiv \frac{k}{\varepsilon} \sqrt{(U_{i,j})^2}$ . Effectively, the  $k\text{-}\varepsilon\text{-}f_P$  EVM has a variable  $C_\mu$ , which is the only difference with the standard  $k\text{-}\varepsilon$  EVM. The scalar function  $f_P$  [11] of the  $k\text{-}\varepsilon\text{-}f_P$  EVM is

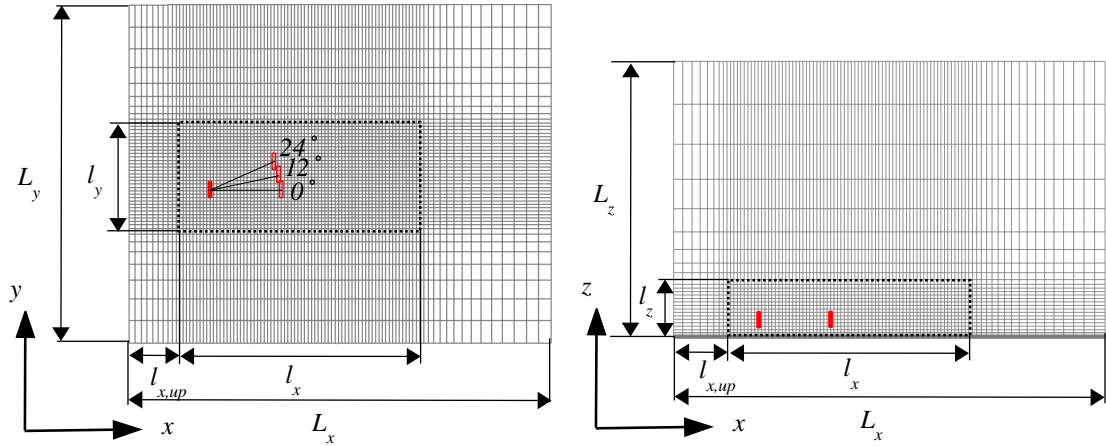


**Figure 7.** General computational domain in RANS simulations. Left: top view. Right: side view. Dashed black box marks the wake domain. ADs are illustrated as red boxes, upstream AD is filled, downstream is not. AD setup shown corresponds to test cases 6 and 7. One in every two nodes is shown.

defined as:

$$f_P(\sigma/\bar{\sigma}) = \frac{2f_0}{1 + \sqrt{1 + 4f_0(f_0 - 1)\left(\frac{\sigma}{\bar{\sigma}}\right)^2}}, \quad f_0 = \frac{C_R}{C_R - 1}, \quad (12)$$

with  $\bar{\sigma}$  as the shear parameter in a log law of the atmospheric boundary layer and  $C_R$  is a calibration parameter. In the log law solution ( $\sigma = \bar{\sigma}$ ),  $f_P = 1$  and for a high shear parameter ( $\sigma > \bar{\sigma}$ )  $f_P < 1$ . High velocity gradients are present in the wake region, which results into a lower turbulent eddy viscosity in the wake predicted by the  $k\text{-}\varepsilon\text{-}f_P$  EVM compared to the one predicted by the  $k\text{-}\varepsilon$  EVM. Hence, the  $k\text{-}\varepsilon\text{-}f_P$  EVM delays the wake recovery.  $C_R$  controls the magnitude of the delayed wake recovery and it is therefore a very important parameter. In previous work [6], the constant  $C_R$  is calibrated against LES for eight different single wind turbine cases. Both the standard  $k\text{-}\varepsilon$  EVM and the  $k\text{-}\varepsilon\text{-}f_P$  EVM use the same transport equations for  $k$  and  $\varepsilon$ :

$$\frac{Dk}{Dt} = \nabla \cdot \left[ \left( \nu + \frac{\nu_T}{\sigma_k} \right) \nabla k \right] + \mathcal{P} - \varepsilon, \quad \frac{D\varepsilon}{Dt} = \nabla \cdot \left[ \left( \nu + \frac{\nu_T}{\sigma_\varepsilon} \right) \nabla \varepsilon \right] + (C_{\varepsilon,1}\mathcal{P} - C_{\varepsilon,2}\varepsilon) \frac{\varepsilon}{k}, \quad (13)$$

where  $\mathcal{P}$  is the turbulent production,  $\nu$  is the kinematic molecular viscosity and  $C_{\varepsilon,1}$ ,  $C_{\varepsilon,2}$ ,  $\sigma_k$ ,  $\sigma_\varepsilon$  are constants. The values of the constants are listed in Table IV.

**Table IV.** Model constants.

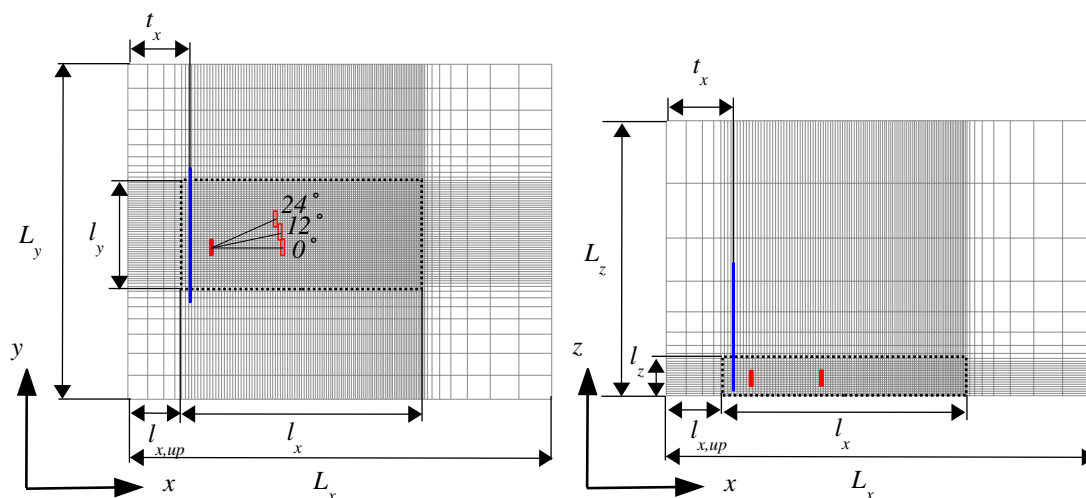
$C_R$	$C_\mu$	$C_{\varepsilon,1}$	$C_{\varepsilon,2}$	$\sigma_k$	$\sigma_\varepsilon$	$\kappa$
4.5	0.03	1.21	1.92	1.00	1.30	0.40

#### 4.1.2. LES

The general flow domain of the LES is shown in Figure 8 and the corresponding dimensions are listed in Table V for each test case. Around the two ADs, a wake domain is defined where the cell spacing is uniformly set in all directions such that the cell size is  $D/30$ . 1.5D upstream of the first AD, synthetic atmospheric turbulence is injected on to a plane that is 8D wide and extends 8D from the bottom. This inflow turbulence is calculated prior to the simulation with the Mann model [35], using a box of with a cross section that is similar to the injection plane. The length of the Mann turbulence box is set to 256D, such that one hour of turbulence plus start up time are generated. The spacing in the Mann turbulence box is  $D/8$  in all directions. Details of the application of Mann turbulence in wind turbine wake simulations can be found in the work of Troldborg et al. [5, 36]. It should be noted that the cell spacings in the wake domain are twice as large as used in previous work [6], hence, a large reduction in computational effort is achieved. A recent grid dependency study of single wind turbine wakes has shown that using a cell size of  $D/30$  in the wake domain is sufficient to resolve the Mann turbulence and wind turbine wake [37]. The total grid size of the grid presented in Figure 8 is 12 million cells.

**Table V.** LES flow domain definition of all test cases. Domain sizes and AD coordinates are normalized by the rotor diameter  $D$ .

Case	Description	Flow domain			Wake domain			Plane	Upstream AD		Downstream AD		
		$L_x$	$L_y$	$L_z$	$l_x$	$l_y$	$l_z$		$l_{x,up}$	$t_x$	$AD_x$	$AD_y$	$AD_x$
Double wake, constant forces, one wind direction													
2-3	NREL 5-MW aligned	25	20	16	14.5	4.4	2	3.25	3.5	5	8	10	8
4-5	NREL 5-MW staggered	25	20	16	14.5	6.9	2	3.25	3.5	5	7.5	9.9	8.5
Double wake, variable forces, relative wind direction range: $-24^\circ, 24^\circ$													
6-7	NREL 5-MW	25	20	16	14.3	6	2	3.25	3.5	5	8.5	variable	variable

**Figure 8.** General computational domain in LES. Left: top view. Right: side view. Dashed black marks the wake domain. ADs are illustrated as a red box, upstream AD is filled, downstream is not. AD setup shown corresponds to test cases 6 and 7. The blue line is the injection plane where the Mann turbulence is imposed. One in every four nodes is shown.

The boundaries at  $x = 0$  and  $z = L_z$  are all inlet boundaries, at which the inlet profiles of equation (8) are imposed. The bottom wall at  $z = 0$  is not resolved by the LES and therefore, a slip wall is specified here. The side boundaries at  $y = 0$  and  $y = L_y$  are also slip walls and an outlet boundary is set at  $x = L_x$ .

The time step is not restricted since the time integration in EllipSys3D is implicit. Although the time step is set to 0.24 s to assure that the unsteady LES data is captured with a high sample frequency.

Details of the LES implementation can be found in the work of Bechmann [38].

## 4.2. Results and Discussion

Table I shows an overview of the comparisons. The results of the three variable AD force methods, for single and double wake simulations, are discussed in Section 4.2.1 and Section 4.2.2, respectively. In these sections, the turbulence is modeled by the  $k\text{-}\varepsilon\text{-}f_P$  EVM. The influence of the turbulence model on the velocity deficit, using constant AD forces, is presented in Section 4.2.3. A similar exercise is conducted in Section 4.2.4, where a variable AD force method is employed to estimate the power deficit.

The results of the LES are made from an average of six ten minute bins and the error bars represent the corresponding standard deviations of the six bins. In addition, all power deficit plots are made from simulations with relative wind directions that range from  $0^\circ$  to  $24^\circ$ . Since the AD is always placed in the cell centers, the simulated wind direction can deviate from the one that is set. Therefore, the simulated wind directions are used in the power deficit plots. The influence of wake rotation on the power deficit is assumed to be small, hence, the results of the negative range of the relative wind directions is simply a mirror image of the simulated positive range.

### 4.2.1. Comparison of variable AD force methods for a single wind turbine

The three variable AD force methods of Section 2 are applied to a single wind turbine for twenty-two undisturbed hub height velocities between 4 m/s and 25 m/s, with a uniform spacing of 1 m/s. The single wind turbine corresponds to test case 1 from Table II. Note that Method III is applied without the  $\tau\text{-}\Omega$  calibration procedure, since  $\Omega$  is known

for single wind turbine simulations. The results of the power curve and the thrust force are compared with the results of two HAWCStab2 [25] aeroelastic computations, as shown in Figure 9. One HAWCStab2 computation is carried out without the blade deflections. Note that the HAWCStab2 computations are not coupled with EllipSys3D. The difference in power and normal force between Method III and the HAWCStab2 simulation with blade deflections is large above rated wind speeds. However, the power and normal force of the HAWCStab2 computation without blade bending compares reasonably well with the CFD, which shows that the effect of the blade deflection is significant above rated wind speeds. In the wind speed range below rated, Method III overpredicts the power compared to HAWCStab2 by 10% to 20%, however, the difference is not caused by the blade deflection because both HAWCStab2 computations show similar results. Réthoré et al. also found that Method III overpredicts the power for a wind speed of 8 m/s. In Method III the local blade force is scaled with the local velocity. Since the velocity gradients are high at the AD location, the sensitivity of location where the local velocity is extracted is high. Réthoré et al. argued that the overprediction in power might be related to the position at which the local velocity is extracted. Method I does not suffer from the severe overprediction in power and normal force above rated wind speeds because it adjusts the forces dynamically, using the local induction. For the wind speeds below rated, Method I still overpredicts the power and the thrust force. The difference is caused by an overprediction of the free-stream velocity by 2%-3% when Equation 4 is applied, which translates to an average error in thrust force and power of  $(1.025^2 - 1) \times 100\% \approx 5\%$  and  $(1.025^3 - 1) \times 100\% \approx 8\%$ , respectively. Method I gives unstable results at a free-stream velocity of 11 m/s, at which the solution is alternating between two equilibrium points during simulation. This phenomenon is not observed in the other two variable AD force methods. Unlike Method III and Method I, Method II predicts the exact same power and normal force as the HAWCStab2 computation with deflection, since it was calibrated to do so.

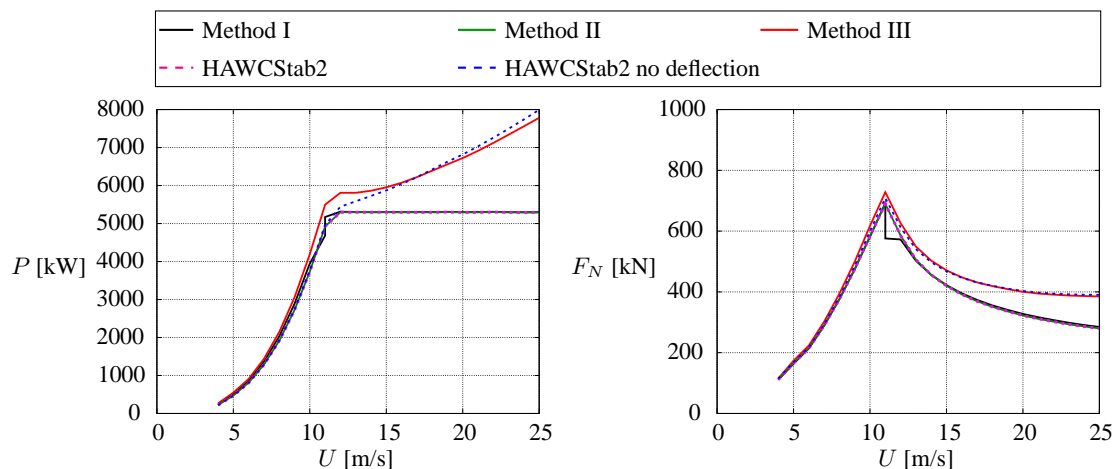


**Figure 9.** Power curve and normal force of the NREL 5-MW wind turbine. Case 1: a single wind turbine with  $I_{H,\infty} = 8\%$ .

#### 4.2.2. Comparison of variable AD force methods for double wakes

The sixth and seventh test case of Table II are used to compare the variable AD force methods for the power prediction of double wakes. In this exercise, only the  $k\text{-}\varepsilon\text{-}f_P$  EVM is employed. In the simulations using Method I (Section 2.1) and Method II (Section 2.2), the power curve and the normal force calculated by Method III are used as an input, instead of the power curve and normal force calculated by HAWCStab2. By doing so, it can be shown that Method III and Method II show the same results in terms of power deficit. In addition, only wind speeds in the zero pitch region are considered, to avoid the necessity of a pitch controller in Method III. Prior to the double wake simulations, a calibration of the alternative scaling coefficients  $C_T^*$ ,  $C_P^*$  and  $\Omega^*$  for Method II is made, as discussed in Section 2.2. In addition, the  $\tau - \Omega$ -relation is derived for Method III, which is explained in Section 2.3.

The power of the downstream wind turbine  $P_2$  and the power ratio of the downstream and upstream  $P_2/P_1$  are plotted in Figure 10. For each variable AD force method, thirteen positive relative wind directions are simulated per test case. The power production of the downstream wind turbine, calculated with Method III and Method II, compares very well. Hence, if airfoil data is not available but  $C_T$ ,  $C_P$  and  $\Omega$  is, Method II is good alternative. Method I overpredicts the power of the downstream wind turbine compared to the other variable AD force methods because the free-stream velocity of the second wind turbine is overpredicted. This result is also observed in the single wind turbine simulations of Section 4.2.1. Surprisingly, all variable AD force methods compare well with respect to the power ratio of the downstream and

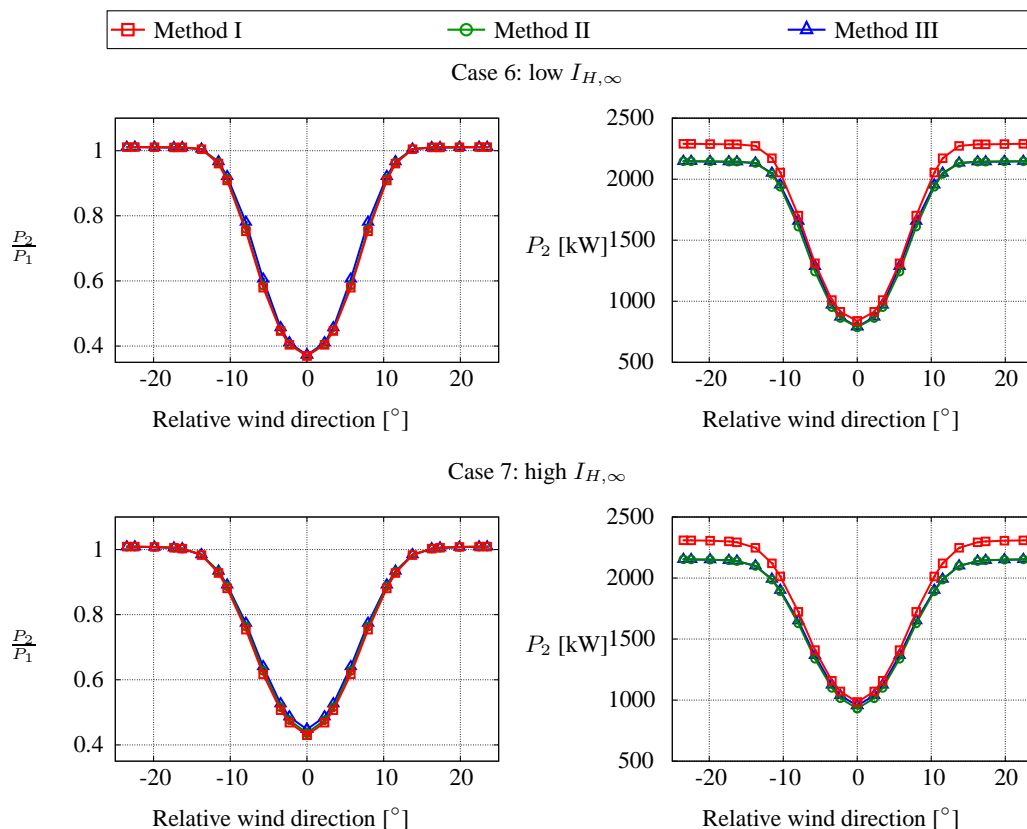


**Figure 10.** Power deficit of the downstream wind turbine. Cases 6 and 7: a double wake with a range of relative wind directions for  $I_{H,\infty} = 4\%$  and  $I_{H,\infty} = 8\%$ , respectively.

upstream wind turbine. Since Method I also overpredicts the power of the upstream wind turbine, the resulting power ratio is comparable with one calculated by the other two variable AD force methods.

As expected, the test case with the lower ambient turbulence intensity shows a larger power deficit compared to the test case with the high ambient turbulence intensity. However, the effect of turbulence intensity on the comparison of the variable AD force methods is negligible.

#### 4.2.3. Comparison of turbulence models for double wakes using constant forces

The  $k\text{-}\varepsilon$  EVM and  $k\text{-}\varepsilon\text{-}f_P$  EVM are compared with LES for double wake configurations using constant forcing. Even though constant AD forces are not realistic for real wind turbines that are operating in wakes of upstream wind turbines, this setup is of interest when testing the RANS based turbulence models. In total, four cases are simulated with all three turbulence models: an aligned and a staggered configuration with a low and a high ambient turbulence intensity. The cases are further described in Section 3. The velocity deficit, the  $f_P$  function and the turbulence intensity are shown in Figures 11, 12 and 13, respectively. The results are extracted over a straight line in the  $y$ -direction, at 2.5D, 5D, 7.5D, 10D and 12.5D downstream from the first AD. Note that the second AD is located at 5D downstream from the first AD.

In the aligned case (cases 2 and 3) from Figure 11, the  $k\text{-}\varepsilon$  EVM underpredicts the velocity deficit at 2.5D with respect to LES, whereas the  $k\text{-}\varepsilon\text{-}f_P$  EVM compares very well with LES. This result is expected since the  $k\text{-}\varepsilon\text{-}f_P$  EVM is calibrated with LES for single wakes. The performance of the  $k\text{-}\varepsilon$  EVM is still poor at 5D. Hence, if a variable AD force method would be used that is based on the local AD velocity, the forcing of the second AD would be much larger in the  $k\text{-}\varepsilon$  EVM compared to the one in the  $k\text{-}\varepsilon\text{-}f_P$  EVM and LES. At 7.5D (2.5D downstream from the second AD), the  $k\text{-}\varepsilon\text{-}f_P$  EVM compares less well with LES, especially for the case with low ambient turbulence (case 2). However, the  $k\text{-}\varepsilon\text{-}f_P$  EVM is still performing better than the standard  $k\text{-}\varepsilon$  EVM. At 10D and 12.5D, the difference between all turbulence models is negligible.

The staggered cases (cases 4 and 5) show similar results as the aligned case at 2.5D. At 5D, a complex velocity profile is visible in which the wake of the first AD is merging with the newly created wake of the second AD. Since the second AD is not in the full wake of the first AD, the velocity deficit of the second AD computed by the  $k\text{-}\varepsilon$  EVM is not much

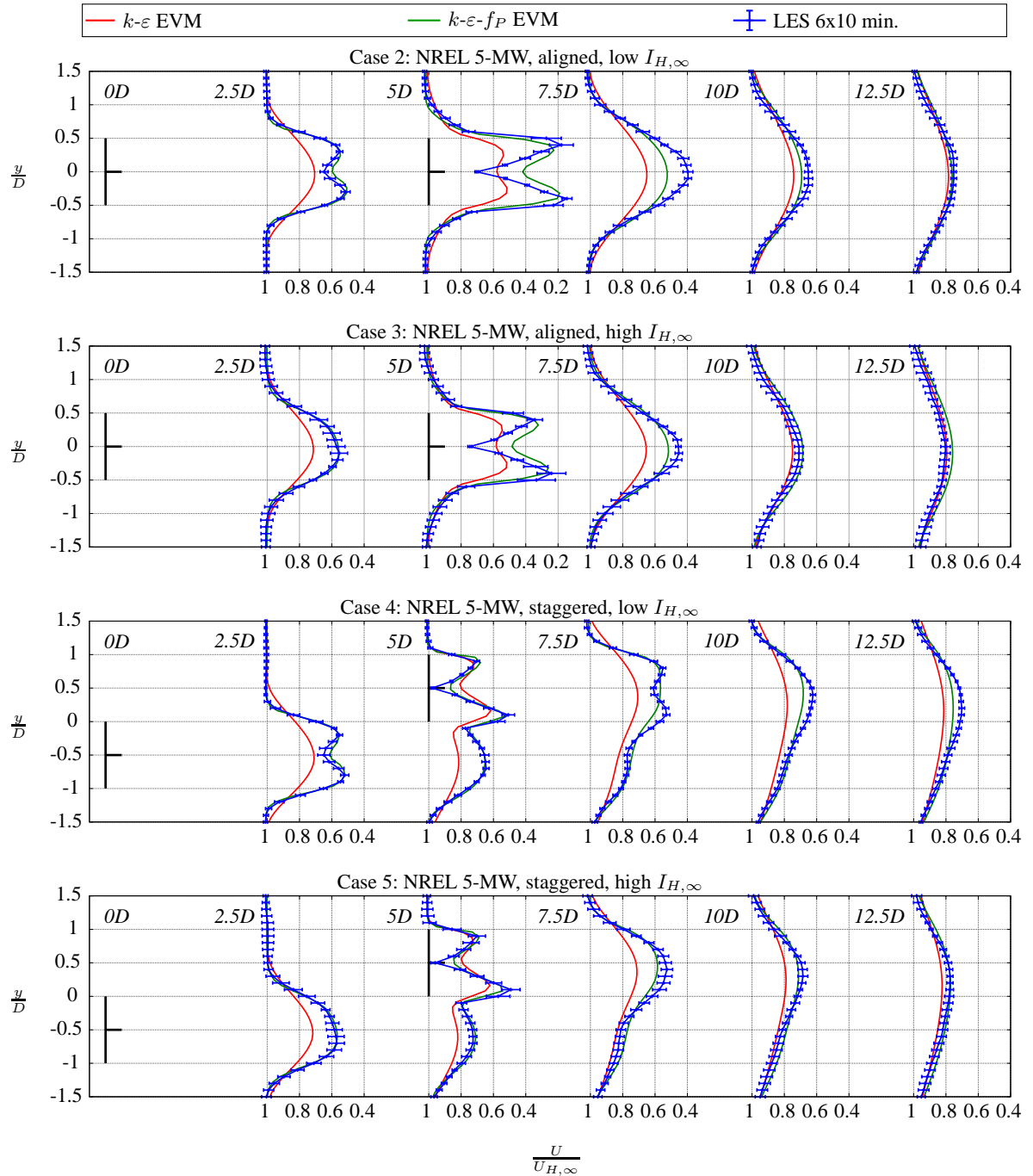


**Figure 11.** Velocity deficit for cases 2-5, a double wake in an aligned and a staggered layout, for  $I_{H,\infty} = 4\%$  and  $I_{H,\infty} = 8\%$ . The LES results include error bars of one standard deviation.

different from the one that is predicted by the  $k-\varepsilon-f_P$  EVM and LES. In contradiction to the aligned cases (cases 2 and 3), the  $k-\varepsilon$  EVM would not underpredict the AD force significantly when a variable AD force method is used. Note that the wake of the first AD at 5D is still underpredicted by the  $k-\varepsilon$  EVM. At 7.5D, the skewed velocity deficit calculated by LES is more complex compared to the RANS based turbulence models, however, the  $k-\varepsilon-f_P$  EVM is still able to approximate it, especially for the high ambient turbulence case. Further downstream in the low ambient turbulence case, at 10D and 12.5D, there are small differences in the predicted velocity deficit of the  $k-\varepsilon-f_P$  EVM and LES. These differences are negligible for the high ambient turbulence case.

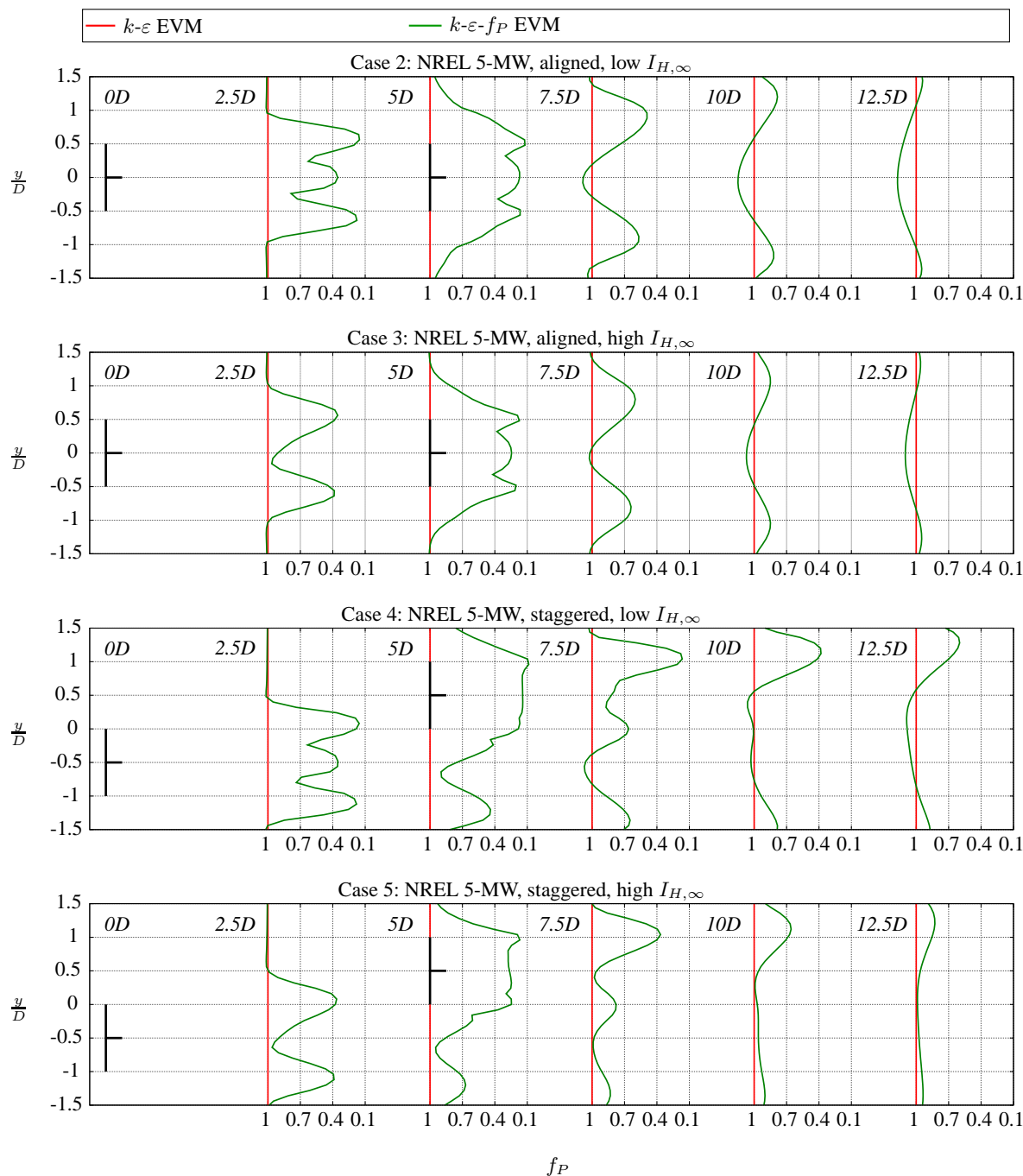


**Figure 12.**  $f_P$  function for cases 2-5, a double wake in an aligned and a staggered layout, for  $I_{H,\infty} = 4\%$  and  $I_{H,\infty} = 8\%$ .

The function  $f_P$ , that represents the varying part of the effective eddy-viscosity coefficient in  $k\text{-}\varepsilon\text{-}f_P$  EVM, as defined in equation (11), is plotted in Figure 12. The results are compared with the  $k\text{-}\varepsilon$  EVM, in which  $f_P$  is equal to one by definition. In the near wake, the value of  $f_P$  is smaller than one, because the velocity gradients are high, especially at the edge of wake. Hence, the eddy viscosity is decreased and the wake recovery is delayed, as observed in Figure 11. The value of  $f_P$  in the near wake is the smallest in the low ambient turbulence cases, because the velocity gradients in the wake are higher when the ambient turbulence intensity is lowered. This explains why the difference in velocity deficit between the  $k\text{-}\varepsilon\text{-}f_P$  EVM and the  $k\text{-}\varepsilon$  EVM is the largest in the low ambient turbulence intensity cases (cases 2 and 4). Further downstream, the  $f_P$  function shows values higher than one, which means that, at these locations, the wake is recovering

faster in the  $k-\varepsilon-f_P$  EVM than the  $k-\varepsilon$  EVM. This behavior of the  $f_P$  function is the cause of the difference in the velocity deficit between the  $k-\varepsilon-f_P$  EVM and LES, in the aligned cases, at 2.5D from the second AD, as seen in Figure 11. The trend in the far wake shows that the  $f_P$  function goes back to one, which explains why the velocity deficit of the  $k-\varepsilon-f_P$  EVM approaches the one of the  $k-\varepsilon$  EVM, at this downstream location.

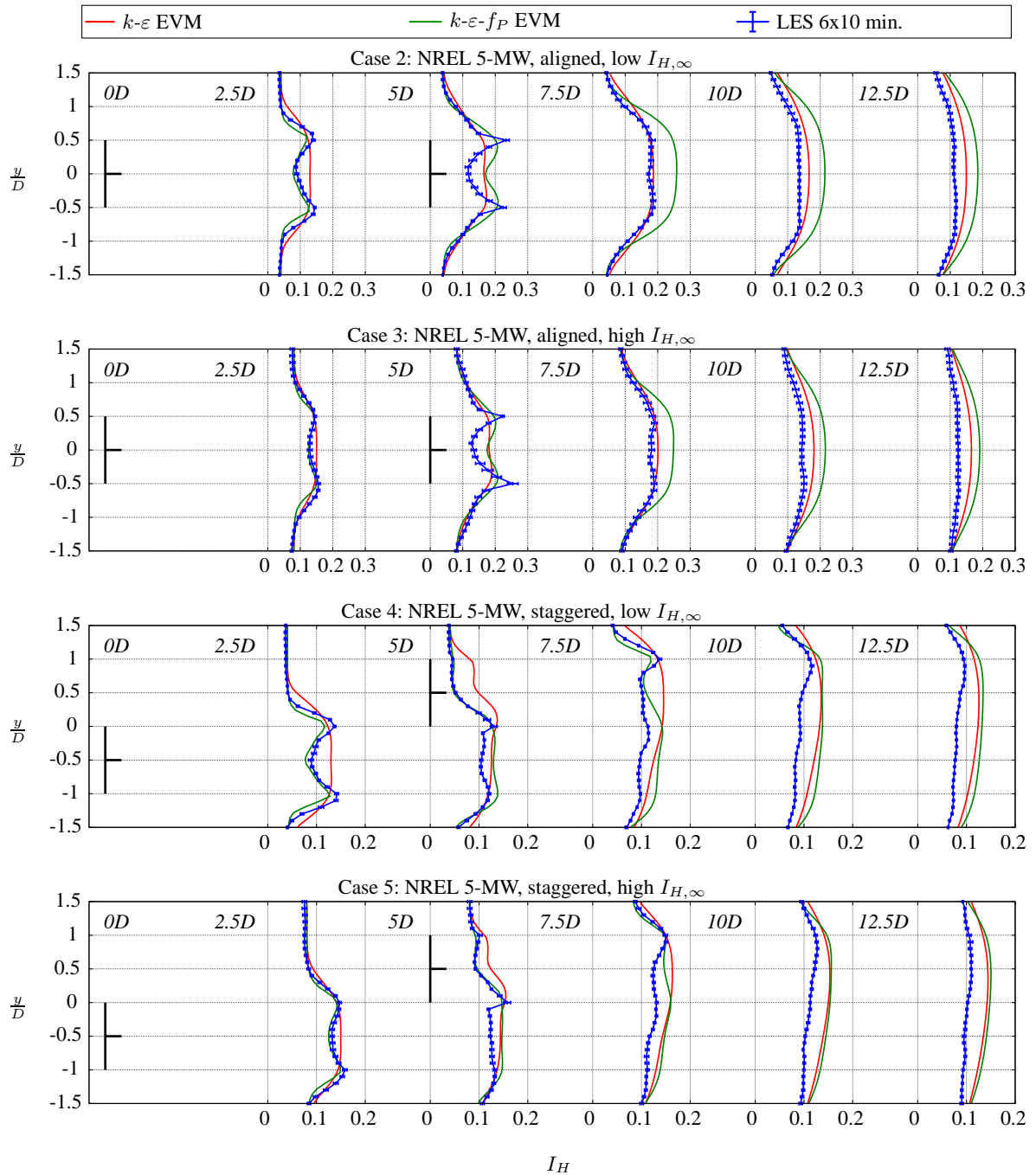


**Figure 13.** Turbulence intensity for cases 2-5, a double wake in an aligned and a staggered layout, for  $I_{H,\infty} = 4\%$  and  $I_{H,\infty} = 8\%$ , respectively. The LES results include error bars of one standard deviation.

The turbulence intensity at hub height  $I_H = \sqrt{2/3k}/U_{H,\infty}$  is shown in Figure 13. The standard  $k\text{-}\varepsilon$  EVM overpredicts the turbulence intensity in the wake center at  $2.5D$  in all cases, compared to LES. This overprediction is also observed for single wake simulations performed in previous work [6, 37], which is caused by the fact that the  $k\text{-}\varepsilon$  EVM produces a non-physical increase in turbulence intensity at  $0D$ , whereas the  $k\text{-}\varepsilon\text{-}f_P$  EVM and LES do not show any added wake turbulence yet. This non-physical increase in turbulence intensity of the  $k\text{-}\varepsilon\text{-}f_P$  EVM at  $0D$ , for single wake simulations, is also visible in the staggered double wake cases at  $5D$  (between  $y/D = 0.5$  and  $y/D = 1$ ), especially for the case with a low ambient turbulence intensity. Both RANS models overpredict the turbulence intensity in the far wake compared to LES. One should keep in mind that the RANS models can only model isotropic turbulence, which is a plausible cause for the overprediction of turbulence intensity of a wake that is characterized by anisotropic turbulence.

#### 4.2.4. Comparison of turbulence models for double wake using variable forces

The double wake test cases, 6 and 7 from Table II, are used to compare the  $k\text{-}\varepsilon\text{-}f_P$  EVM with the standard  $k\text{-}\varepsilon$  EVM and LES, for one variable AD force method. To avoid the need of expensive calibrations in the LES for Method II and Method III, the simple AD Induction is employed. In Figure 14, the power production of the downstream wind turbine and the power ratio of the downstream and the upstream wind turbine are plotted against the simulated relative wind directions. In terms of absolute power of the downstream wind turbine, the  $k\text{-}\varepsilon\text{-}f_P$  EVM compares well with LES, also outside the wake of the downstream wind turbine. On the contrary, the  $k\text{-}\varepsilon$  EVM shows a larger power of the downstream wind turbine outside the wake region, which is caused by an overpredicted  $\langle U_{AD} \rangle$ . This indicates that the axial induction, predicted by the  $k\text{-}\varepsilon$  EVM, does not compare well with the one of the  $k\text{-}\varepsilon\text{-}f_P$  EVM and LES. The power deficit of the downstream wind turbine is underpredicted by the  $k\text{-}\varepsilon$  EVM, which is best visible in the plots of the power ratio. In the comparison of the turbulence models with constant AD forces (Section 4.2.3), it is observed that the velocity deficit is underpredicted by the  $k\text{-}\varepsilon$  EVM. This translates into an underprediction of the power deficit in Figure 14. The  $k\text{-}\varepsilon$  EVM performs the worst for the low ambient turbulence case, which is also seen in the comparison with the constant AD forces from Section 4.2.3. The power deficit of the  $k\text{-}\varepsilon\text{-}f_P$  EVM compares very well with the one of LES, especially for the low ambient turbulence case. The variable  $C_\mu$ , that is present in the  $k\text{-}\varepsilon\text{-}f_P$  EVM, establishes the improvement by lowering the eddy-viscosity in the near wake region.

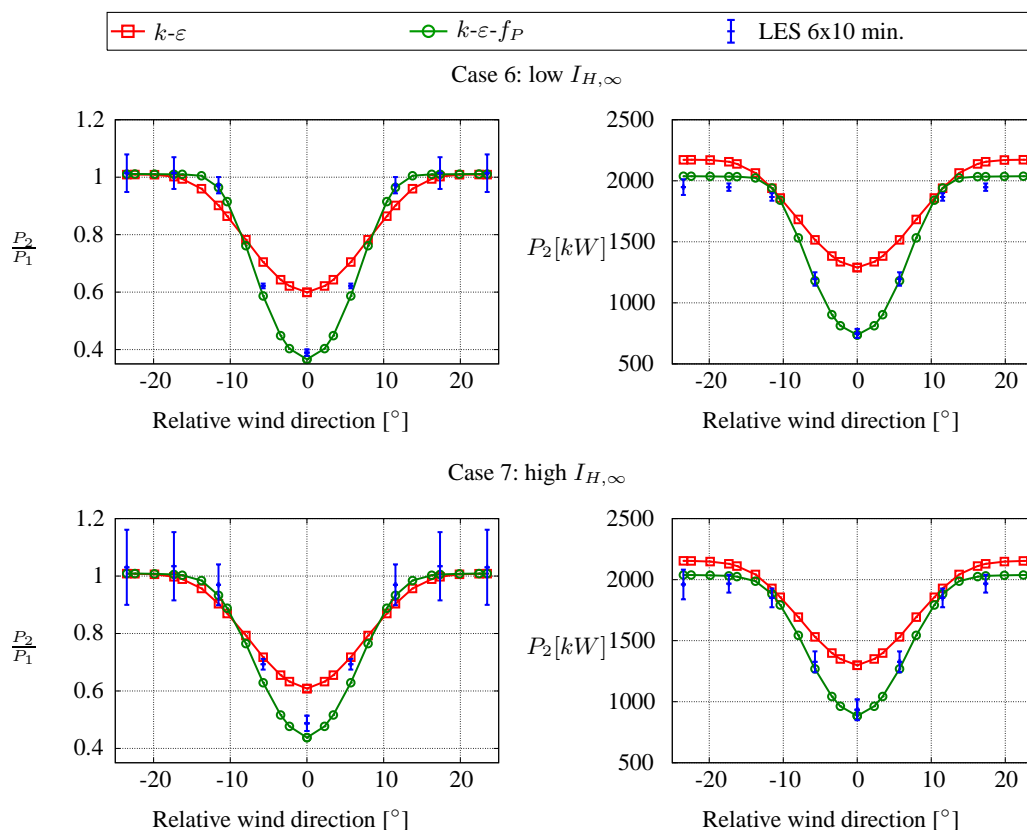


**Figure 14.** Power deficit of the downstream wind turbine. Cases 6 and 7: a double wake with a range of relative wind directions for  $I_{H,\infty} = 4\%$  and  $I_{H,\infty} = 8\%$ , respectively. The LES results include error bars of one standard deviation.

## 5. CONCLUSIONS

Two existing variable AD methods; the AD Induction Method (Method I) and the AD Airfoil Method (Method III), are compared with the proposed AD Variable Scaling Method (Method II), for single and double wake simulations, employing the  $k-\varepsilon-f_P$  EVM. Compared to the aeroelastic code HAWCStab2, Method III without torque calibration overpredicts the power and the thrust force of a single wind turbine, for wind speeds above rated, because blade deflections are not included. For wind speeds below rated, Method III calculates the correct total thrust force but still overpredicts the power by 10%-20%. Method I overpredicts the power and the thrust force below rated wind speeds, because the dynamically predicted undisturbed velocity at hub height is overpredicted by 2%-3%. On the contrary, the proposed Method II produces the exact same results as HAWCStab2 because the method relies on calibration. This exercise shows that Method II is flexible because it can be used to fit any reference  $C_T$ ,  $C_P$  and  $\Omega$ .

When the power and the thrust force, predicted by Method III for a single wind turbine, are used as an input for Method I and Method II, the results of Method III and Method II compare very well, for double wake simulations. This shows that when airfoil data is not available but information about  $C_T$ ,  $C_P$  and  $\Omega$  is, Method II is a good alternative. In the double wake configuration, the power ratio predicted by Method I compares well with Method III and Method II, because Method I overpredicts the power of both the upstream and the downstream wind turbines by a similar factor. Therefore, if only the power ratio of the upstream and downstream wind turbine is desired, the simple Method I is an acceptable method. On the contrary, if accurate absolute power is needed only the proposed Method II can be used. It should be noted that numerically unstable behavior is observed for one of the simulations employing Method I, because the solution of local velocity at the AD oscillated between two converged values. In other words, the solution of the local velocity at the AD is not unique. This behavior has not been seen in the other two variable AD force methods.

The performance of the  $k-\varepsilon$  EVM and the  $k-\varepsilon-f_P$  EVM is tested against LES for six double wake cases with different wind turbine positions and ambient turbulence intensities. Four cases are simulated with constant AD forces and two cases are carried out with variable AD forces, using Method I. The cases with constant forces show that the  $k-\varepsilon$  EVM underpredicts the velocity deficit in the near wake and at the location of the downstream wind turbine compared to LES, especially for low ambient turbulence and in full wake conditions. On the contrary, the  $k-\varepsilon-f_P$  EVM shows comparable velocity deficits with LES. When the wind turbines are staggered, the velocity deficit at the downstream wind turbine, calculated with the  $k-\varepsilon$  EVM is similar to the one of the  $k-\varepsilon-f_P$  EVM and LES, because the downstream wind turbine is not operating in full wake conditions. In addition, at 7.5D downstream of the second wind turbine the difference between  $k-\varepsilon$  EVM and the  $k-\varepsilon-f_P$  EVM is small and both models show similar velocity deficits. The turbulence intensity in the wake is overpredicted by both RANS models, however, the  $k-\varepsilon-f_P$  shows a comparable turbulence intensity with LES in the near wake.

The underpredicted velocity deficit at location of the downstream wind turbine, calculated by the  $k-\varepsilon$  EVM in full wake conditions, translates into an underpredicted power deficit in the test cases with variable AD forces. In addition, the  $k-\varepsilon$  EVM overpredicts the absolute power outside the wake region compared to results of the  $k-\varepsilon-f_P$  EVM and LES. This is caused by the fact that Method I uses the axial induction to predict the power and that the axial induction predicted by the  $k-\varepsilon$  EVM does not correspond to one calculated by  $k-\varepsilon-f_P$  EVM and LES.

From the present work, it can be concluded that the best setup for double wake RANS simulations is the use of the proposed Method II together with the  $k-\varepsilon-f_P$  EVM. Hence, the correct thrust force and power is calculated, inside and outside the wake region.

## ACKNOWLEDGEMENTS

This work is supported by the Center for Computational Wind Turbine Aerodynamics and Atmospheric Turbulence funded by the Danish Council for Strategic Research, grant number 09-067216. Computational resources were provided by DCSC and the DTU central computing facility.

## REFERENCES

1. Barthelmie RJ, Hansen K, Frandsen ST, Rathmann O, Schepers JG, Schlez W, Philips J, Rados K, Zervos A, Politis ES, *et al.*. Modelling and measuring flow and wind turbine wakes in large wind farms offshore. *Wind Energy* 2009; **12**:431–444.
2. Jensen LE. Array efficiency at Horns Rev and the effect of atmospheric stability. *EWEC, Milan, Italy*, 2007.
3. Jensen NO. A note on wind generator interaction. *Technical Report Risø-M-2411*, Risø National Laboratory, Roskilde, Denmark 1983.

4. Churchfield MJ, Lee S, Moriarty PJ, Martinez LA, Leonardi S, Vijayakumar G, Brasseur JG. A Large-Eddy Simulation of Wind-Plant Aerodynamics. *AIAA conference, Nashville, USA*, 2012.
5. Troldborg N, Larsen GC, Madsen HA, Hansen KS, Sørensen JN, Mikkelsen R. Numerical simulations of wake interaction between two wind turbines at various inflow conditions. *Wind Energy* 2011; **14**:859–876.
6. van der Laan MP, Sørensen NN, Réthoré PE, Mann J, Kelly MC, Troldborg N, Schepers JG, Machefaux E. An improved  $k\text{-}\varepsilon$  model applied to a wind turbine wake in atmospheric turbulence. *Wind Energy* Published online, 2014; .
7. Réthoré PE. Wind Turbine Wake in Atmospheric Turbulence. PhD Thesis, Risø 2009.
8. El Kasmi A, Masson C. An extended  $k\text{-}\varepsilon$  model for turbulent flow through horizontal-axis wind turbines. *Journal of Wind Engineering and Industrial Aerodynamics* 2008; **96**:103–122.
9. Prospathopoulos JM, Politis ES, Rados KG, Chaviaropoulos PK. Evaluation of the effects of turbulence model enhancements on wind turbine wake predictions. *Wind Energy* 2011; **14**:285–300.
10. Cabezón D, Migoya E, Crespo A. Comparison of turbulence models for the computational fluid dynamics simulation of wind turbine wakes in the atmospheric boundary layer. *Wind Energy* 2011; **14**:909–921.
11. Apsley DD, Leschziner MA. A new low-Reynolds-number nonlinear two-equation turbulence model for complex flows. *International Journal of Heat and Fluid Flow* 1998; **19**:209–222.
12. Mikkelsen R. Actuator Disc Methods Applied to Wind Turbines. PhD Thesis, Technical University of Denmark, Mek dept 2003.
13. Réthoré PE, van der Laan MP, Troldborg N, Zahle F, Sørensen NN. Verification and validation of an actuator disc model. *Wind Energy* 2013; Published online.
14. Troldborg N, Zahle F, Sørensen NN, Réthoré PE. Comparison of wind turbine wake properties in non-uniform inflow predicted by different rotor models. *Torque conference 2012, Oldenburg, Germany*, 2012.
15. Troldborg N, Zahle F, Sørensen NN, Réthoré PE. Comparison of wind turbine wake properties in non-sheared inflow predicted by different CFD rotor models. *Wind Energy* 2013; Submitted, May 2013.
16. Calaf M, Meneveau C, Meyers J. Large eddy simulation study of fully developed wind-turbine array boundary layers. *Physics of Fluids* 2010; **22**:015 110.
17. Wu YT, Porté-Agel F. Large-Eddy Simulation of Wind-Turbine Wakes: Evaluation of Turbine Parametrisations. *Boundary-Layer Meteorology* 2011; **138**:345–366.
18. Jonkman J, Butterfield S, Musial W, Scott G. Definition of a 5-MW Reference Wind Turbine for Offshore System Development. *Technical Report*, National Renewable Energy Laboratory 2009.
19. Porté-Agel F, Wu YT, Lu H, J CR. Large-eddy simulation of atmospheric boundary layer flow through wind turbines and wind farms. *Journal of Wind Engineering and Industrial Aerodynamics* 2011; **99**:154–168.
20. Sørensen JN, Shen WZ. Numerical modelling of wind turbine wakes. *Journal of Fluids Engineering* 2002; **124**:393–399.
21. Shen WZ, Mikkelsen R, Sørensen JN, Bak C. Tip loss corrections for wind turbine computations. *Wind Energy* 2005; **8**:457–475.
22. Shen WZ, Sørensen JN, Mikkelsen R. Tip loss corrections for Actuator/Navier-Stokes computations. *Solar Energy Engineering* 2005; **127**:209–213.
23. Troldborg N. Personal communication 2014; .
24. Wu YT, Porté-Agel F. Modeling turbine wakes and power losses within a wind farm using LES: An application to the Horns Rev offshore wind farm. *Proceeding for the ICOWES2013, Copenhagen, Denmark*, 2013; 537–548.
25. Hansen MH. Aeroelastic properties of backward swept blades. *49th AIAA Aerospace Sciences Meeting including the New Horizons Forum and Aerospace Exposition, Orlando, Florida*, 2011.
26. Dahlberg JÅ. Assessment of the Lillgrund windfarm. *Technical Report*, Vattenfall Vindkraft AB 2009.
27. Sørensen NN. General purpose flow solver applied to flow over hills. PhD Thesis, Technical University of Denmark 1994.
28. Michelsen JA. Basis3d - a platform for development of multiblock PDE solvers. *Technical Report AFM 92-05*, Technical University of Denmark, Lyngby 1992.
29. Patankar SV, Spalding DB. A calculation procedure for heat, mass and momentum transfer in three-dimensional parabolic flows. *International Journal of Heat and Mass Transfer* 1972; **15**:1787–1806.
30. Leonard BP. A stable and accurate convective modelling procedure based on quadratic upstream interpolation. *Computer Methods in Applied Mechanics and Engineering* 1979; **19**:59–98.
31. Réthoré PE, Sørensen NN. A discrete force allocation algorithm for modelling wind turbines in computational fluid dynamics. *Wind Energy* 2012; **15**:915–926.
32. Rhie CM, Chow WL. Numerical study of the turbulent flow past an airfoil with trailing edge separation. *AIAA Journal* 1983; **21**:1525–1532.
33. Launder BE, Spalding DB. *Mathematical models of turbulence*. Academic Press, London, UK, 1972.

34. Boussinesq MJ. *Théorie de l'écoulement tourbillonnant et tumultueux des liquides*. Gauthier-Villars et fils, Paris, France, 1897.
35. Mann J. The spatial structure of neutral atmospheric surface-layer turbulence. *Journal of Fluid Mechanics* 1994; **273**:141–168.
36. Troldborg N, Sørensen JN, Mikkelsen R, Sørensen NN. A simple atmospheric boundary layer model applied to large eddy simulation of wind turbine wakes. *Wind Energy* 2014; **17**:657–669.
37. van der Laan MP, Storey RC, Sørensen NN, Norris SE, Cater JE. A CFD code comparison of wind turbine wakes. *Submitted to Torque conference*, 2014.
38. Bechmann A. Large-Eddy Simulation of Atmospheric Flow over Complex Terrain. PhD Thesis, DTU-MEK, Denmark 2007.